Advanced Steel Construction – Vol. 21 No. 4 (2025) 316–326
DOI:10.18057/IJASC.2025.21.4.4

SEISMIC PERFORMANCE OF END-PLATE CONNECTION IN A NARROW-FLANGE H-SHAPED BEAM-COLUMN

Wei-Hui Zhong [1, 2, *], Di Wu [1], Zheng Tan [1, 2], Ying-Zhao Qiu [1], Dong-Ping Yang [1], Chen-Hao Ren [3] and Le Deng [1]

[1] *School of Civil Engineering, Xi'an University of Architecture and Technology, Xi'an 710055, China*
[2] *Key Lab of Structural Engineering and Earthquake Resistance, Ministry of Education, Xi'an University of Architecture and Technology, Xi'an 710055, China*
[3] *Shaanxi Architecture Science Research Institute Company Limited, Xi'an 710082, China*
** (Corresponding author: E-mail: Email: zhongweihui1980@163.com)*

ABSTRACT

To improve the seismic performance of both low-rise and multi-story steel residential structures, and to address the ongoing issue of column protrusion, this paper introduces a cross-shaped end-plate connection joint. This joint is designed for narrow-flange H-beams and has been evaluated through quasi-static tests for failure modes, hysteresis curves, and load-bearing capacity. Experimental findings indicate that this joint serves as a semi-rigid connection, offering exceptional ultimate rotational capacity, energy dissipation, and ductility. These features make it well-suited for use in mid- and low-rise seismic steel frame structures. To deepen our understanding of the joint's seismic performance, a numerical model was established using ABAQUS software. The validity of this modeling approach was confirmed by comparing it with experimental results. Several variables were analyzed for their impact on the joint's seismic performance, including axial compression ratio, column web thickness, skin plate thickness, column-flange reinforcement plate thickness, and beam end-plate thickness. Our analysis reveals that an increase in the axial compression ratio makes the negative slope of the joint's hysteresis curve more pronounced. This suggests that the axial compression ratio should not exceed 0.4. Additionally, the use of skin plates led to a 26.3% increase in joint yield displacement and a 14.9% increase in ultimate displacement. The incorporation of column-flange reinforcement plates boosted both the yield and peak strength by 15.5% and 14.2%, respectively. Consequently, we recommend using skin and reinforcement plate thicknesses that are 0.5 and 0.8 times the thickness of the end-plate, respectively. By carefully selecting the appropriate parameters for these components, this study offers valuable insights and guidelines for the practical implementation of beam-column joints in low-rise and multi-story steel residential structures.

ARTICLE HISTORY

Received: 9 March 2024
Revised: 15 January 2025
Accepted: 6 February 2025

KEYWORDS

Narrow-flange H-shaped
Beam column;
End-plate connections;
Seismic performance;
Prefabricated structures

1. Introduction

In the context of a strong push for green, low-carbon, and energy-efficient building structures, steel frame systems and light steel truss systems have gained widespread use in low-rise and multi-story steel residential structures [1]. However, these types of buildings often face challenges, including reduced lateral stiffness of frame columns and the awkward positioning of wide-flange columns that protrude from walls. These issues affect not only aesthetic appeal of the interior spaces but also the efficient use of architectural space [2]. In low and medium-rise steel frame structures, the vertical load-bearing members are subjected to relatively small loads. Utilizing wide-flange H-beam columns in such cases may lead to material wastage and encroachment on the wall, thereby negatively impacting its aesthetics. Therefore, this paper suggests employing narrow-flange load-bearing members in low and medium-rise steel frame structures. To mitigate the problem of protruding columns, narrow-flange columns can be effectively utilized in mid- and low-rise buildings.

To date, the majority of academic research has focused on the seismic performance of wide- and medium-flange beam-column connections in the strong-axis direction. For instance, Wang [3] introduced a detachable end-plate connection with a cruciform structure, finding that factors such as end-plate thickness and the column's width-to-thickness ratio had a significant impact on connection performance. D'Aniello et al. [4] employed finite element analysis to discover that adding stiffening ribs to end plates could substantially improve their strength and stiffness. They also examined the performance of beam-column connections under various conditions. Haghollahi et al. [5] performed experimental research to identify performance trends in connections both with and without stiffening ribs. Van-Long et al. [6] proposed an extended end-plate connection method for linking I-beams to externally wrapped composite columns, using the component method for simulation.

Other scholars have focused on specialized areas. Chen [7] examined beam-column end-plate connections in portal frames and found that thickening the web plates in the connection zone was more beneficial than adding diagonal stiffening ribs. Guo et al. [8] designed and conducted experiments on eight different beam-column end-plate connections, concluding that bolted end-plate connections showed excellent ductility and energy dissipation capacity. Li et al. [9] experimented with externally extended end-plate connections of varying configurations. They found that the relative strengths of bolts, end plates, and column walls directly affected the failure modes of the joints. Yan [10] introduced a linear model for calculating the initial stiffness of semi-rigid connection joints, while Tong [11] presented an enhanced end-plate stiffening technique and developed design formulas for externally extended end-plate stiffeners.

In contrast to wide- and medium-flange beam-column connections, which have larger height-to-thickness ratios, narrow-flange connections display greater stiffness in the weak-axis direction. This leads to notable differences in seismic performance between narrow-flange beam-column connections and their wide- or medium-flange counterparts. While some research exists on narrow-flange connections, studies focusing on their seismic performance in the strong-axis direction are relatively limited. Zhong et al. [12] investigated a specific narrow-flange beam-column end-plate weak-axis connection joint and found that factors such as beam end-plate and skin plate thicknesses significantly affect the joint's seismic performance.

Although numerous scholars have explored the performance of narrow-flange beam-column connections, research specifically targeting their seismic performance in the strong-axis directions remains limited. To address the issue of flange exposure and further investigate the seismic performance of narrow-flange H-section steel beam-column end-plate connections in the strong-axis direction, this paper introduces a cross-shaped joint configuration for narrow-flange H-beam-column connections. We subjected full-scale beam-column connection specimens to quasi-static tests to evaluate their failure modes, hysteresis curves, and overall seismic performance. Utilizing finite element analysis and corroborating the results with experimental data, we ensured the validity of our modeling method. A comprehensive parametric analysis was conducted, focusing on factors such as the axial compression ratio, column web thickness, skin plate thickness, column-flange reinforcement plate thickness, and beam end-plate thickness. This analysis aimed to provide deeper insights into the key parameters affecting the seismic performance of the proposed joint. Based on our findings, we offer design recommendations that serve as a foundational guide for engineering applications.

2. Joint design

2.1. The selection of substructures

In compliance with the Chinese Steel Structure Design Standard GB 50017-2017[13], we designed a two-story steel frame prototype structure featuring a 2 × 2 span configuration. The structure has a floor height of 3 m, a span of 3.9 m, a permanent floor load of 3.1 kN/m^2, and a live load of 2 kN/m^2. We selected the bottom-level central column in the strong-axis direction (BP-5) of the prototype structure as the subject of our study, as illustrated in Fig. 1. The cross-shaped joint structure was arranged in a double-half-span configuration, comprising a failing column flanked by connected steel beams. Typically, the column's moment of flexural failure occurs at the midpoint of the inter-story height; thus, we chose a length of 2.4 m for the failing column. For the beams, the moment of flexural failure generally occurs around half the beam span, leading us to select a length of 1.6 m for one side of the beam.

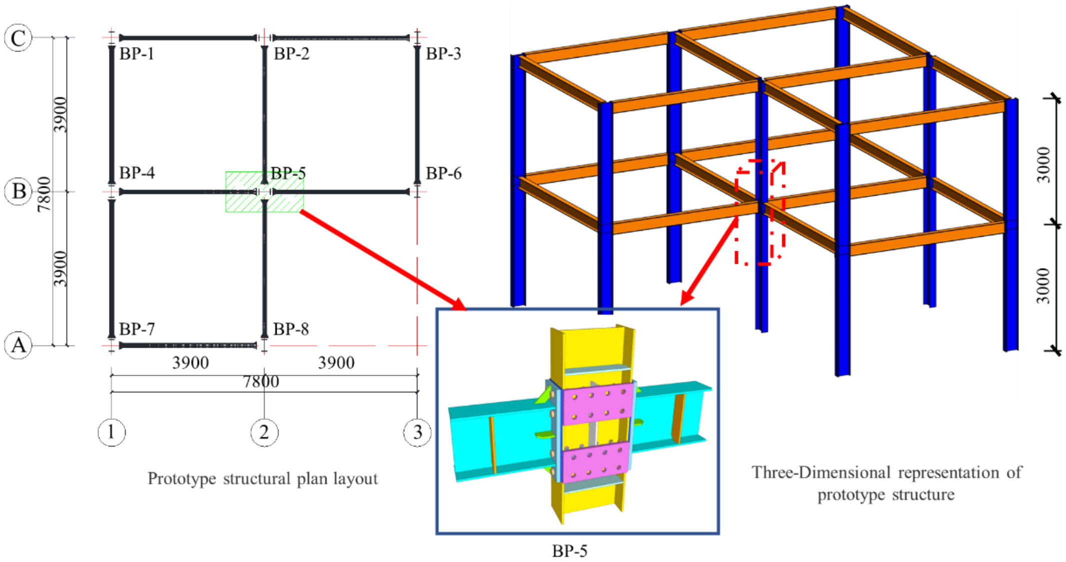

Fig. 1 Prototype steel frame structure

2.2. Experimental specimen design

2.2.1. Joint structural design

This paper proposes a novel structural concept for narrow-flange H-section steel beam-column connections, featuring an extended end-plate bolted joint. The specific configuration of this connection is depicted in Fig. 2. The external extended end-plate design allows for energy dissipation through end-plate deformation, resulting in excellent hysteresis behavior and energy dissipation capacity [14]. Furthermore, the inclusion of stiffening ribs on the beam end-plate enhances both its strength and stiffness, facilitating a more uniform load distribution on the bolts and improving bolt tension distribution.

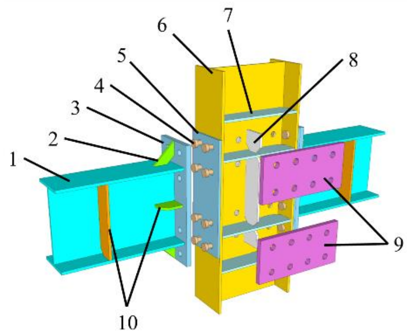

1. Beam; 2. End-plate stiffening rib; 3. End-plate;
4. High-strength bolt; 5. Column-flange reinforcement plate; 6. Column;
7. Column transverse stiffeners; 8. Column longitudinal stiffeners; 9. Skin plate;
10. Beam stiffening rib

Fig. 2 Narrow-flange extension end-plate bolted joint

Adding transverse and longitudinal stiffeners in the joint region not only improves the joint's stiffness and strength but also effectively distributes its load-bearing capacity, markedly enhancing local buckling behavior. Additionally, the incorporation of skin plates in the weak-axis direction fortifies the beam-column joint region. This serves a dual purpose: it both safeguards the joint and preserves the aesthetic integrity of the building walls. The design accommodates connections in the weak-axis direction, with a skin plate thickness equal to that of the beam end-plate.

2.2.2. End-plate and bolt design

In the realm of end-plate connection joint design, Solhmirzaei et al. [15] constructed two bolted end-plate joints and compared their performance against the bolted stiffened end-plate with four bolts reinforcement (BSEEP-16ES) standard recommended by AISC 4-358 [16]. Their investigation showed that the custom-designed joints demonstrated superior seismic resistance capabilities. Tartaglia [17] compared the AISC 358-16 guidelines with European standards, demonstrating that stiffened end-plate joints can ensure the formation of plastic hinges in steel beams under cyclic loading conditions. This research also explored the use of four-row bolted connections for beams with and without stiffening ribs. Following a similar approach, our study employs a four-row bolt configuration for the connections.

In compliance with the Chinese structural technical standard GB 51022-2015 [18], we opted for Grade 10.9 M16 high-strength friction-type bolts with an 18 mm bolt hole diameter. Bolt dimensions were determined based on the tension transmitted through the beam's end flange, as calculated according to the Chinese steel structure design standard GB50017-2017 [13].

2.2.3. Dimension design of specimens

Due to the advantages of ease in both fabrication and experimental loading, our test specimens were designed and constructed as full-scale models. The steel beam and column sections have specifications of HN250 × 125 × 6 × 9 (mm) and HN300 × 150 × 6.5 × 9 (mm) [H-overall depth (d) × flange width (b_f) × web thickness (t_w) × flange thickness (t_f)], and are made of Q235B-grade steel, as depicted in Fig. 3(a).

2.2.4. Skin plate design

Regarding the design of skin plates, Lu [19] proposed a technique involving the use of skin plates to connect steel beams to H-shaped columns in the weak-axis direction. This allows the structural components to fail before the joints do. These skin plates were designed in accordance with the permissible bolt hole spacing values specified in the Chinese steel structure standard GB 50017-2017 [13]. Positioned at the same horizontal level as the edge of the end plates in the column's height direction, the skin plates align flush with the flanges on either side of the column in the width direction. To prevent localized damage to the column's narrow flange, skin plates were introduced in the weak-axis direction to ensure a uniform load distribution and uniform stiffness. The thickness of the upper and lower skin plates is informed by the thickness of both column flanges and the web plate. The thickness of these plates typically falls between the thicknesses of the web plate and the column flanges. For this study, we selected a skin plate thickness of 16 mm, as shown in Fig. 3(b).

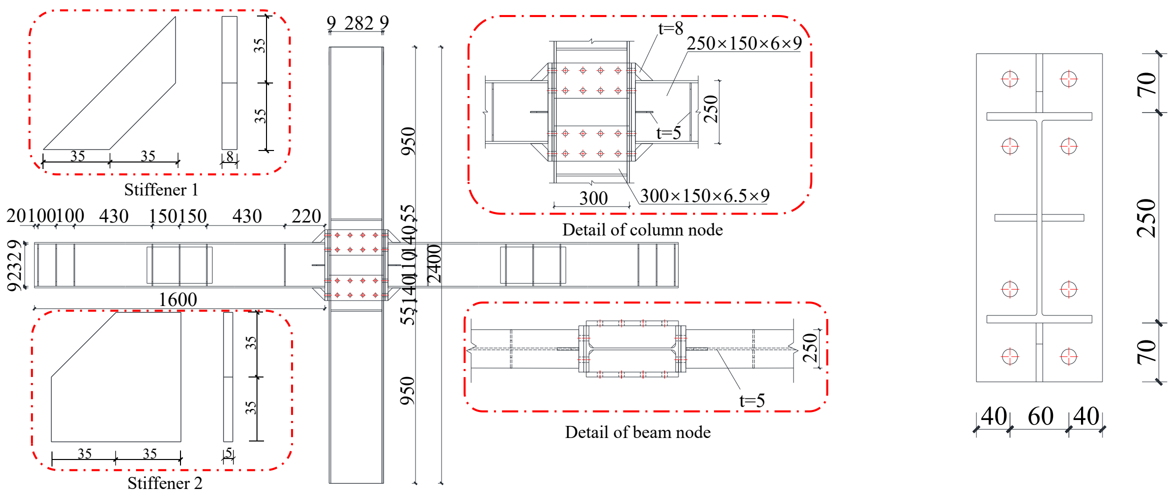

(a) Detailed geometric dimensions of the specimen (b) End-plate size

Fig. 3 Geometric dimension drawing of the specimen

2.3. Joint verification

In this work, we focus on BP-5, as illustrated in Fig. 1. Calculations reveal that the axial compression ratio of BP-5 is approximately 0.2. The following sections present a detailed seismic assessment of this joint:

2.3.1. Seismic structural measures calculation

Designed to withstand a predicted seismic intensity of 8 degrees, the steel frame is categorized as Level III for seismic performance according to the Chinese Building Seismic Design Code GB50011-2010 [20] . The aspect ratios of the frame's columns meet the design criteria, and the verification are shown in Eqs. (1) and (2):

$$l_0 / i_x = 3000/124 = 24.19 \le 100\sqrt{235/f_y} = 100 \tag{1}$$

$$l_0 / i_y = 3000/32.9 = 91.19 \le 100\sqrt{235/f_y} = 100 \tag{2}$$

In accordance with the Chinese Building Seismic Design Code GB50011-2010 [20], we calculated and verified the width-to-thickness ratio limits for various components within the steel frame. The calculations confirm compliance with the code's requirements.

2.3.2. Component verification

To ensure that the beam fails before the column, we increased the column's stiffness and designed its moment capacity to enhance its resistance to failure and bending strength. The aim is to have the beam yield prior to the column, forming plastic hinges at the beam ends, as defined by Eq. (3).

$$\sum W_{pc}\left(f_{yc} - N_p / A_c\right) \ge \eta \sum W_{pb} f_{yb} \tag{3}$$

where w_{Pc} and w_{Pb} signifies the plastic section moduli of the column and beam at the joint, respectively; f_{yc} and f_{yb} denote the yield strengths of the steel used in the column and beam, respectively; N_P represents the axial force in the column for the seismic combination; and A_c is the column's cross-sectional area. Further, η represents the strong column coefficient, with values of 1.15 for the first level, 1.10 for the second level, and 1.05 for the third level.

According to Eq. (3), the computed plastic moment at the column-end exceeds that at the beam-end (189.88 kN·m > 164.34 kN·m), thereby ensuring that the beam fails before the column does.

3. Experimental synopsis

3.1. Material property analysis

Material property testing was carried out in accordance with the relevant Chinese standard GB/T2975-2018 [21], and the resulting steel material performance indicators are detailed in Table 1.

Table 1
Material properties of specimens

Steel member	Yield strength f_y/MPa	Tensile strength f_u/MPa	Elastic modulus E/GPa	Elongation percentage %
Beam web	430	562	207	32
Column web	285	408	208	39
Beam-end reinforcement plate	295	435	185	40
Beams, column flange	242	390	239	43
End-plate, skin plate	298	462	204	53
Beam-end web stiffener ribs	472	585	219	28

3.2. Experimental procedure

3.2.1. Experimental apparatus setup

The experimental loading setup, shown in Fig. 4(a), positioned the test specimen between two gantry frames. A servo actuator was horizontally affixed to the reaction wall. The bottom of the test specimen was connected to a ground beam via a hinge axis. This ground beam was longitudinally placed between the two gantry frames and anchored securely to both sides using anchor bolts. Additional stabilization was provided by four compression beams. A hydraulic jack on the reaction beam applied vertical pressure to the columns, maintaining a strictly downward direction. The column base was linked to the hinge axis to replicate the column's flexural point. At the beam-end, a connection was made through a bracket and linkage, with the opposite end of the linkage fastened to the ground beam, as shown in Fig. 4(b). Lateral supports were installed at the mid-section of both the joint and loading beam to prevent out-of-plane instability during loading, as illustrated in Fig. 4(c).

3.2.2. Experimental loading procedure

The experimental loading approach utilized a hybrid load–displacement method. Initially, a vertical load of 200 kN was applied to the column's top to account for second-order gravity effects. Next, horizontal reciprocating loads were applied to the top of the column. The horizontal cyclic loading had two stages: the first stage involved load-controlled conditions, with the yielding load incrementally distributed over three steps—16, 32, and 48 kN—each subjected to one complete cycle. The second stage was displacement-controlled; after reaching the yield point, the loading increased in increments of 0.5 times the yield displacement (20 mm) for each level. Each level went through three complete cycles, and the loading continued until specimen failure, as outlined in Fig. 5.

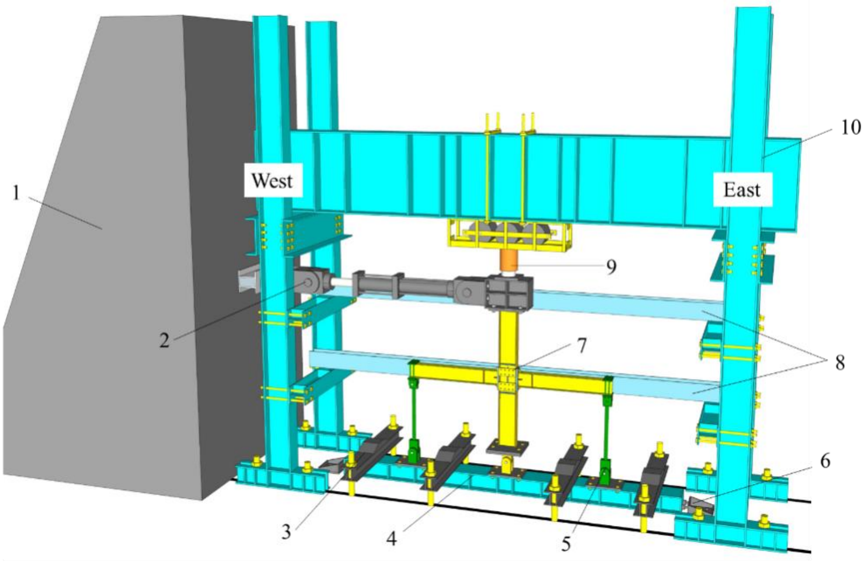

1. Reaction wall；2. MTS servo actuator；3 Pressed beam；4. Floor beams；5. Chain rod；6. Anchor bolts；7. Test piece；8. Side beams；9. Jack；10. Mastry

(a) Test the loading device

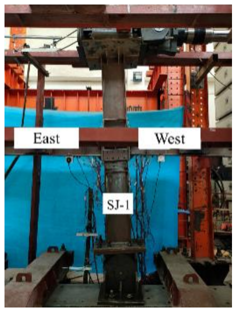

(b) Front of the test device

(c) Side of the test device

Fig. 4 Experimental device

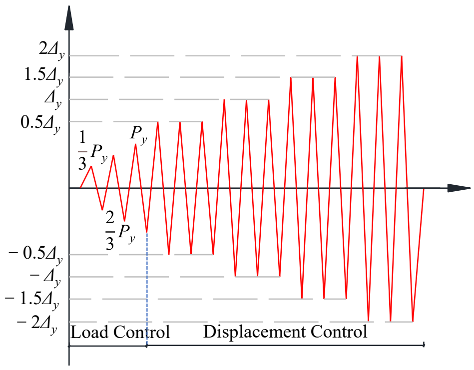

Fig. 5 Experimental loading system

3.3. Sensor placement

The experimental measurement parameters mainly encompassed column-end displacements, beam-column joint rotations, beam-column flange strains, beam-column web strains, and stiffener strains, among others. The arrangement of the displacement sensors is displayed in Fig. 6(a). Relative rotations between the columns and beams were measured and are labeled as W1–W4. Displacement sensors W5 and W7 were situated at the top and bottom of the column, respectively. Sensor W6 was designated to monitor any sliding between the hinge axis and the ground beam.

Strain gauges were used to quantify the strains on the beam flanges, beam webs, column flanges, and beam webs, as illustrated in Fig. 6(b). Due to the specimen's symmetry, only one half is illustrated, with corresponding symmetric measurement points indicated in parentheses.

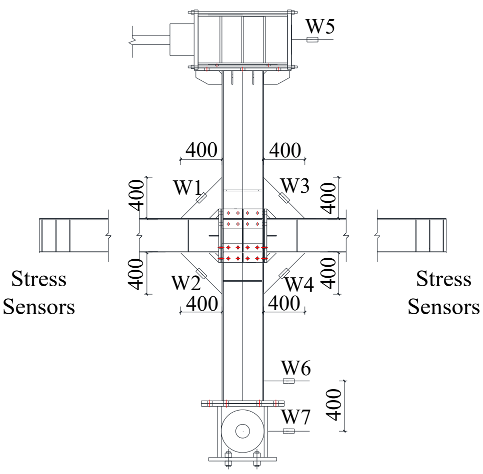

(a) Displacement meter layout drawing

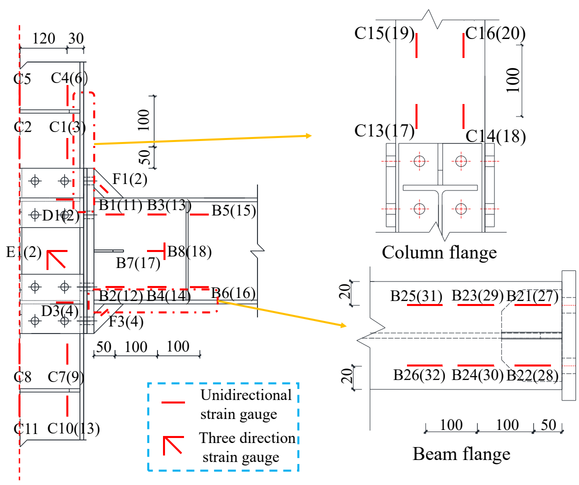

(b) Strain gauge arrangement in the beam and column nodal area

Fig. 6 Measurement point arrangement of beam and column joint data

4. Experimental results and analysis

4.1. Experimental curves and failure modes

The load–displacement hysteresis curve for specimen SJ-1 is depicted in Fig. 7. This curve shows basic symmetry in both the positive and negative directions and exhibits a pronounced pinched shape. A gradual decline in both load-bearing capacity and stiffness indicates that the specimen demonstrated strong plastic deformation and energy dissipation abilities. No evident signs were observed during the early stages of loading. However, at point A (75 mm, 58 kN), significant shear deformation became visible in the nodal region, as captured in Fig. 8(a). At point B (-135 mm, -68 kN), localized buckling manifested in the stiffener at the east side of the beam's end-plate, as shown in Fig. 8(b). upon reaching point C (175 mm, 68 kN), the tension-side end-plate stiffener on the east side detached, illustrated in Fig. 8(c). At point D (-184 mm, -63 kN), a marked increase in end-plate deformation was evident, as shown in Fig. 8(d). Ultimately, when the load reached point E (196 mm, 45 kN), the load-bearing capacity fell below 85% of the peak load, signaling the end of the loading process.

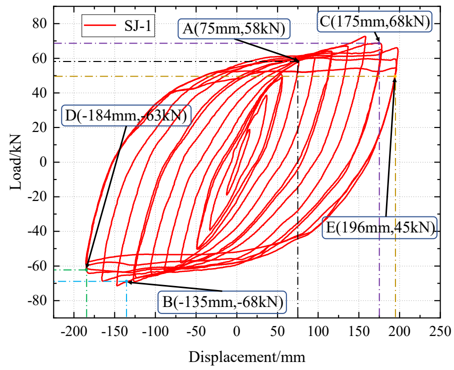

Fig. 7 Load–displacement hysteresis curve

(a) Joint domain shear deformation

(b) End-plate stiffener is locally buckled

(c) End-plate stiffener is disconnected

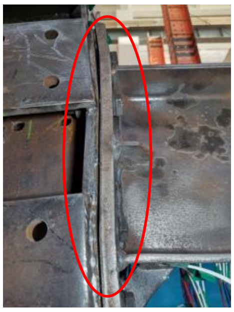

(d) Deformation of the end-plate is significantly increased

Fig. 8 Test phenomenon of specimens

During the experiment, after the stiffener on the end-plate fractured, the end-plate displayed noticeable deformation and showed weld-seam fractures at its junction with the beam flange. This outcome suggests that the end-plate stiffeners effectively augment the stiffness of the end-plate, thereby delaying the occurrence of weld-seam fractures between the end-plate and the beam flange. The inter-story displacement angle at the specimen's point of failure was 0.045 rad, substantially exceeding the 0.02 rad limit for elastic–plastic interlayer displacement angles in rare seismic events, as specified in the Chinese "Code for Seismic Design of Buildings" (GB50011-2010) [20]. This highlights the specimen's exceptional rotational capacity, signaling its superior seismic performance.

4.2. Strain analysis of specimen components

The strain of each member of the specimen joint is shown in Fig 9, the positive value is the tensile stress, the negative value is the compressive stress, and the measurement points are: the steel beam flange is 50mm away from the end plate (Q1), the steel column flange is 100mm away from the end plate (Q2), the skin plate (Q3), the column joint domain (Q4), and the end plate stiffener (Q5).

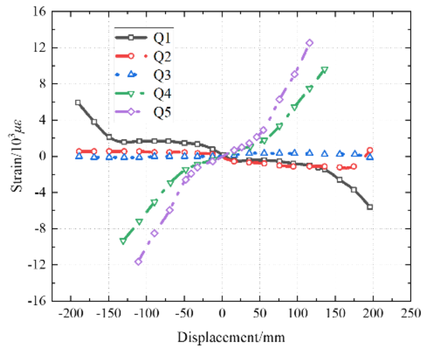

Fig. 9 Displacement–strain curve of the specimen

This study investigated the behavior of various specimen components under different loading conditions. The yielding sequence in the experimental joint unfolded as follows: initial yielding was evident in the end-plate stiffener, followed by shear yielding in the column joint area, and finally, yielding occurred in the beam flange situated 50 mm from the end-plate. Despite its small size, the end-plate stiffener initially exhibited subtle yielding with local buckling becoming conspicuous only after significant plastic deformation had occurred. Following the fracture of the stiffener on the end-plate, a considerable increase in strain was observed in the beam flange, culminating in its eventual yielding. These observations are consistent with the strain data obtained experimentally.

4.3. Skeleton curve analysis

The curve illustrating the bending moment–rotation relationship of the joint offers a comprehensive insight into the mechanical performance of the beam-column joints. As depicted in Fig. 10, the experimental joints transition through distinct phases of elasticity, plasticity, and failure. In the initial stages of loading (phases A–D), the bending moment at the joint increased linearly with the rotation angle. Upon yielding (phases A–B and D–E), the rate of moment growth moderated, and the M–θ curve exhibited significant nonlinearity. During the joint's failure stages (phases B-C and E-F), the load-bearing capacity declined to 85% of the peak load. The ultimate rotation angle of the joint was 0.045 rad, substantially exceeding the 0.03 rad rotational capacity specified by the American LRFD code for special moment-frame joints under cyclic testing [22]. With an initial rotational stiffness of 23,364.78 kN·m, the joint falls within the stiffness classification range of ($0.5EI_b/L_b$, $25EI_b/L_b$) as defined in the code, classifying it as a semi-rigid joint.

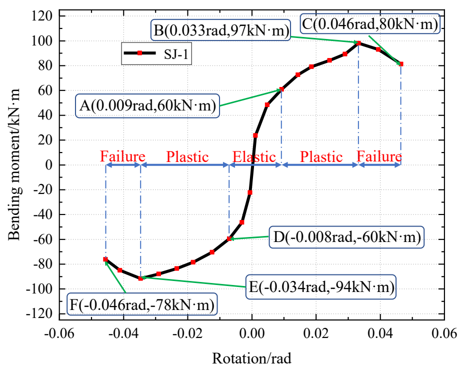

Fig. 10 Skeleton curve

4.4. Stiffness degradation

The secant stiffness K_i serves as an indicator of stiffness degradation in specimens under cyclic loading. Its calculation formula, Eq. (4), is as follows:

$$K_i = \frac{|+F_i| + |-F_i|}{|+X_i| + |-X_i|} \tag{4}$$

where F_i represents the load value at the first-cycle peak during the ith level of loading for the specimen, and X_i corresponds to the displacement value at this peak point.

As computed using Eq. (4), the stiffness degradation curve for the experimental component is presented in Fig. 11. Point A (18 mm, 1.37 kN·mm^{-1}) marks the initial secant stiffness of the joint. As loading progressed, the secant stiffness exhibited a gradual decline. Due to earlier yielding in both the end-plate stiffener and the nodal region, a noticeable dip in stiffness occurred near point B (55 mm, 0.95 kN·mm^{-1}). The stiffness curve showed a consistent reduction, without abrupt changes. When it reached point C (55 mm, 0.95 kN·mm^{-1}), the secant stiffness at the ultimate displacement indicated that the joint maintains relatively stable stiffness characteristics.

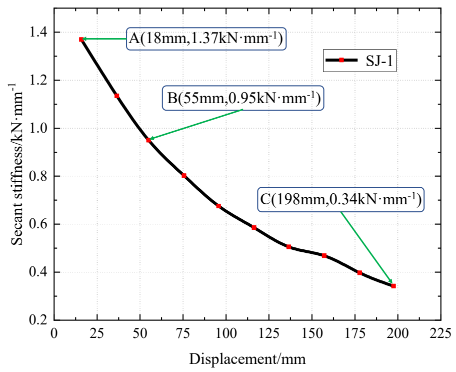

Fig. 11 Stiffness degradation curve of secant line of the specimen

4.5. Energy dissipation capacity of joints

This study also assessed the energy dissipation capacity of the specimens using the equivalent viscous damping coefficient (h_e). The area under the curve is depicted in Fig. 12 and was determined using Eq. (5):

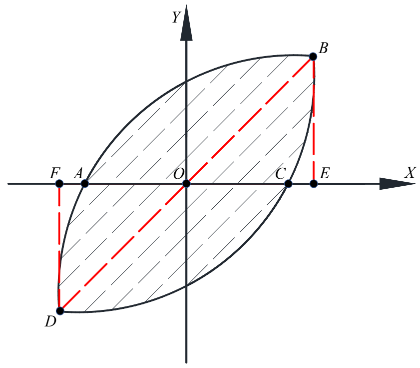

Fig. 12 Calculation of equivalent viscous damping coefficient

$$h_e = \frac{1}{2\pi} \cdot \frac{S_{(ABC+CDA)}}{S_{(OBE+ODF)}} \tag{5}$$

where $S_{(ABC+CDA)}$ represents the area enclosed by the hysteresis loop within one cycle, and $S_{(ABC+ODF)}$ denotes the triangular area corresponding to one cycle.

As illustrated in Fig. 13, the behavior during the initial loading phase, fell within the elastic regime, with the initial equivalent viscous damping coefficient (h_e) positioned at point A (18 mm, 0.09). As the load continued to increase, stress in certain components transitioned to the elastic–plastic range, leading to enhanced energy dissipation. Consequently, h_e increased in a stepwise manner. The maximum h_e for the final test specimen was at point B (198 mm, 0.43), demonstrating that the joint has excellent energy dissipation capacity.

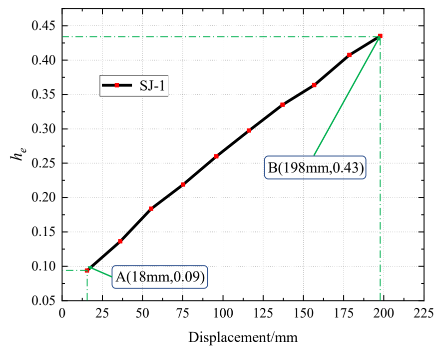

Fig. 13 Equivalent viscous damping coefficient

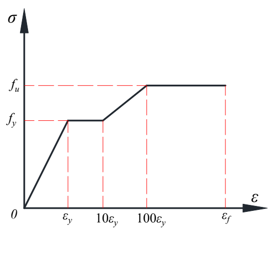

(a) Steel stress–strain curve

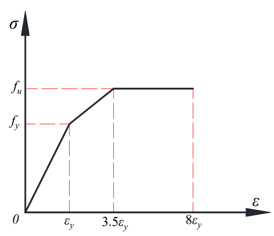

(b) Bolt stress–strain curve

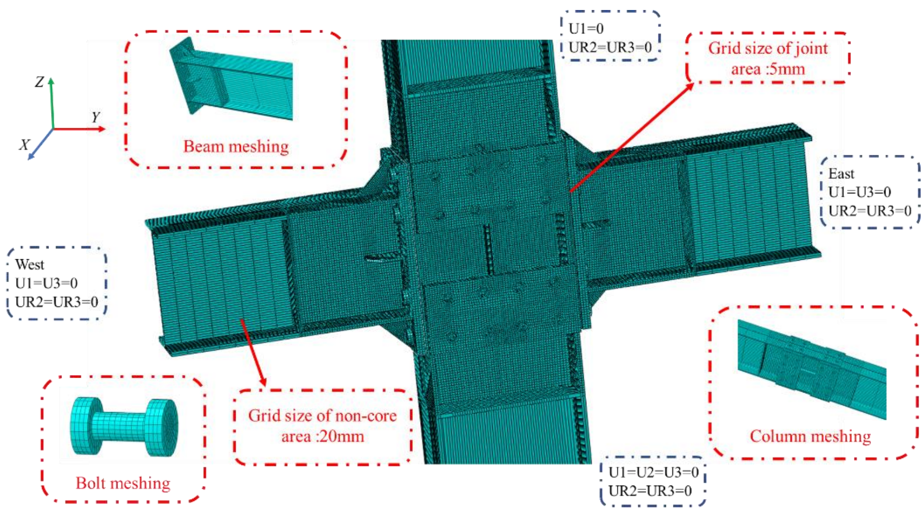

(c) Finite element model and its joint mesh

Fig. 14 Finite element modeling

5. Finite element model analysis

5.1. Establishment of finite element models

This study employed the ABAQUS/Standard static implicit method for finite element analysis on a narrow-flange H-shaped beam-column joint model. The finite element model mirrored the geometric dimensions and boundary conditions of the experimental specimens. To capture the true essence of the experimental data, the model incorporated the behavior of steel under cyclic loading conditions. A dynamic strengthening criterion was applied, and a bilinear constitutive model was chosen to replicate the steel's behavior [23], as shown in Fig. 14(a). In addition, a trilinear constitutive model was used to mimic the behavior of bolts [24], as detailed in Fig. 14(b). The material's Poisson's ratio was set at 0.3, and ductile metal failure criteria were implemented to simulate steel fractures [25]. Parameters such as fracture strain, triaxial stress, and strain rate were defined to simulate the steel fractures within the finite element software. General contact boundary conditions [26] were applied to the interfaces between various elements such as the bolt shaft and bolt hole wall, the nut and connecting end-plate, and column flange, as well as the end-plate and the column flange. In the normal direction, hard contact was defined, and a coefficient of friction of 0.3 was used. This model has not considered the impact of initial defects. Tangential direction contact was defined as Coulomb friction, with friction calculations conducted via the penalty method. Additionally, tie constraints were applied to simulate the welded connections.

The finite element model, complete with boundary constraints, is depicted in Fig. 14(c). In order to more accurately replicate the experimental observations, C3D8R solid elements were used and mesh sensitivity analysis was performed to refine the regions with complex stress patterns.

5.2. Validation of finite element models

Comparison between numerical simulation results and experimental observations including failure modes, hysteresis curves, and skeleton curves are illustrated in Figs. 15 and 16. The model closely matched the experimental findings, particularly in the tearing of the weld joint between the column-flange stiffener plate and the column flange, accompanied by localized buckling at the beam-end. Overall, the finite element simulation results were in strong alignment with the experimental data, capturing the joint's yielding behavior with high accuracy. This discrepancy between the finite element and experimental hysteresis and skeleton curves was below 10%. This level of agreement between the finite element simulation results and the experimental outcomes validates the robustness and accuracy of our finite element modeling approach, confirming its aptness for parameter analysis.

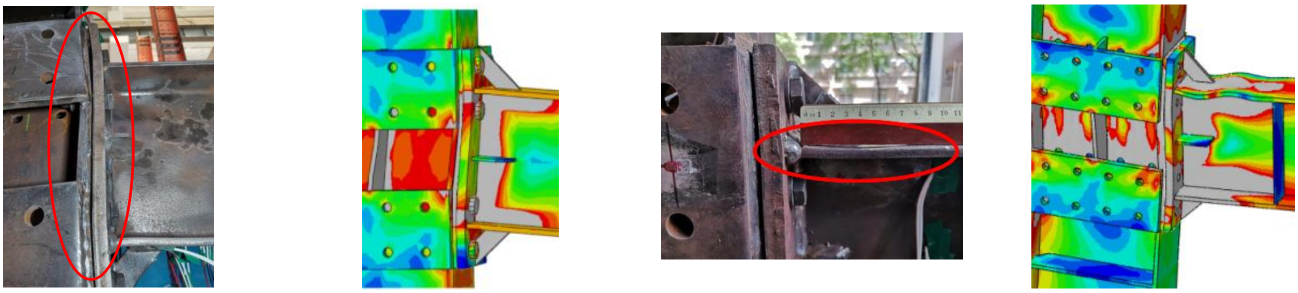

(a) End-plate is bent and deformed

(b) Beam flange is locally buckled

Fig. 15 Comparison of finite element simulation and experimental failure patterns

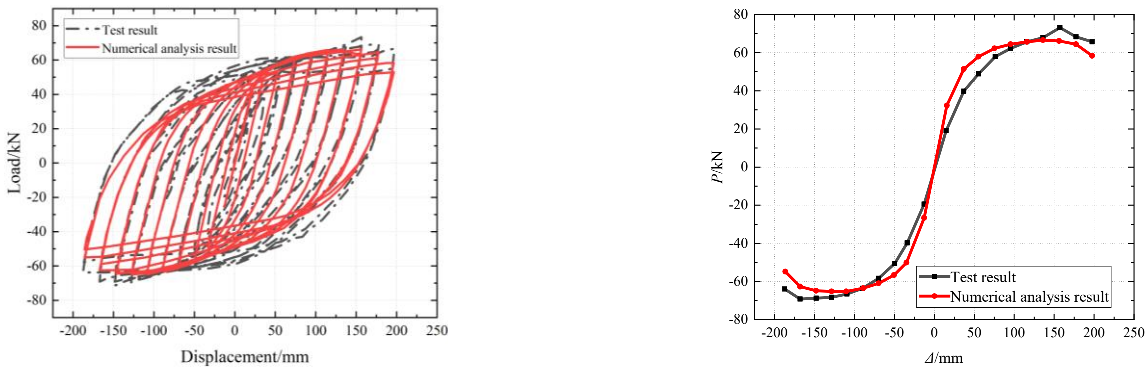

(a) Hysteresis curve

(b) Skeleton curve

Fig. 16 Comparison between finite element and test

6. Parameter analysis

6.1. Selection of test specimen parameters

Expanding on the finite element modeling approach detailed in Section 4.1, we conducted a comprehensive parameter analysis focusing on key variables. These variables included the axial compression ratio (ACR), thickness of the column web (TCW), thickness of the skin plate (TSP), thickness of the column-flange stiffener plate (TFS), and the beam end-plate thickness (BEP). The aim was to investigate their impact on vital performance metrics such as load-carrying capacity, deformability, energy dissipation capacity, and seismic performance. Table 2 presents these parameters, with “BASE” serving as the reference model for comparison.

6.2. Influence of axial compression ratio

The hysteresis curves, skeleton curves, and mechanical performance of the ACR series finite element models are presented in Fig. 17 and Table 3. The ACR series exhibited distinct spindle-shaped hysteresis loops, signaling excellent energy dissipation attributes. Starting with model ACR-2, a negative slope emerged in the hysteresis loop, signaling performance degradation in the frame. This is attributed to increased displacement, which amplifies the second-order effect of P-Δ in the specimens. The negative slope of the joint hysteresis curve is an indication of frame performance degradation.

Upon increasing the ACR, we observed a modest decline in the initial stiffness across the specimens. For instance, for those with an ACR of 0.7, the initial stiffness dipped by 9.7% when compared to the BASE specimen, which has an ACR of 0.2. Therefore, the ACR had a relatively minor influence on the structural stiffness under standard operating conditions. However, its impact on ductility was more conspicuous. Specifically, for the ACR-5 model, the ductility coefficient diminished by 33.5% compared to the BASE specimen. This suggests that the ACR considerably affects both load-bearing and deformation capacities. Accordingly, we recommend stringent control of the ACR during the design stage. For structures expected to experience lateral displacements, it would be prudent to cap the ACR at 0.4 when utilizing this type of joint.

Table 2
Model parameters of each joint

Model number	Axial compression ratio	Column web thickness /mm	Skin plate thickness /mm	Strengthen plate thickness /mm	End-plate thickness /mm
BASE	0.2	6.5	16	8	16
ACR-1	0.3				
ACR-2	0.4				
ACR-3	0.5	6.5	16	8	16
ACR-4	0.6				
ACR-5	0.7				
TCW-1	0.2	8	16	8	16
TCW-2		10			
TSP-1			8		
TSP-2	0.2	6.5	4	8	16
TSP-3			2		
TSP-4			0		
TFS-1				0	
TFS-2				4	
TFS-3	0.2	6.5	16	12	16
TFS-4				16	
TFS-5				20	
BEP-1					12
BEP-2					20
BEP-3	0.2	6.5	16	8	24
BEP-4					28
BEP-5					32

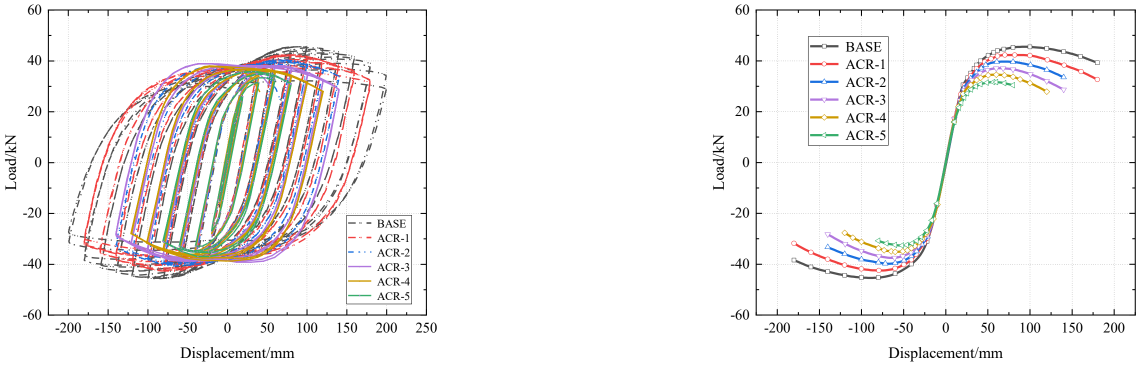

(a) Comparison of ACR series P–Δ hysteresis curves

(b) Comparison of ACR series hysteresis skeletons

Fig. 17 Comparison of ACR series hysteresis curve and skeleton

Table 3
Bearing capacity, displacement, and ductility of ACR series specimens

Model number	Initial stiffness kN/mm^{-1}	Yield load P_y/kN	Yield displacement Δ_y/mm	Peak load P_{max}/kN	Limit displacement Δ_u/mm	Ductile coefficient μ
BASE	1.75	37.91	35.02	45.41	181.97	5.19
ACR-1	1.73	35.56	32.56	42.44	158.55	4.87
ACR-2	1.69	33.49	30.42	39.68	138.74	4.56
ACR-3	1.67	31.58	28.48	37.33	121.89	4.28
ACR-4	1.63	29.60	26.63	34.84	109.22	4.10
ACR-5	1.58	27.26	24.40	31.77	81.20	3.32

6.3. Impact of column web thickness

The hysteresis curves, skeleton curves, and mechanical performance of the TCW series and the BASE model are displayed in Fig. 18 and Table 4. Our findings indicate that the BASE and TCW-1 specimens demonstrate strong energy dissipation, evident from their stable and well-defined spindle-shaped hysteresis curves. In contrast, the TCW-2 model, while exhibiting a higher initial load-bearing capacity, shows a quicker decline in that capacity.

A closer look at the TCW series reveals that compared to the BASE model, TCW-1 and TCW-2 experienced yield load increases of 10.31% and 22.95%, respectively. However, their ultimate displacements diverged by 6.2% and -25.6% from the BASE specimen. This data suggests that an increase in the thickness of TCW leads to compromised ductility at the joints. Consequently, we recommend a column web thickness of 8 mm to maintain adequate joint ductility.

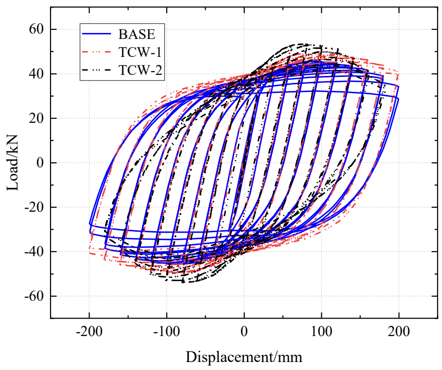

(a) Comparison of TCW series *P–Δ* hysteresis curves

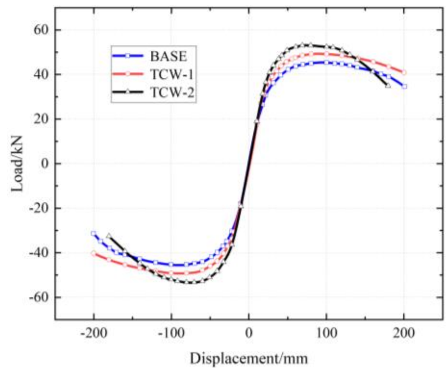

(b) Comparison of TCW series hysteresis skeletons

Fig. 18 Comparison of TCW series hysteresis curve and skeleton

Table 4
Bearing capacity, displacement, and ductility of TCW series specimens

Model number	Initial stiffness kN/mm^{-1}	Yield load P_y/kN	Yield displacement Δ_y/mm	Peak load P_{max}/kN	Limit displacement Δ_u/mm	Ductile coefficient μ
BASE	1.75	37.91	35.03	45.41	181.97	5.19
TCW-1	1.82	41.82	35.29	49.19	193.20	5.47
TCW-2	1.89	46.61	35.96	53.32	144.90	4.03

6.4. Influence of skin plate thickness

Turning to the TSP series, Fig. 19 and Table 5 outline the hysteresis curves, skeleton curves, and mechanical properties of these finite element models. These curves progress through elastic, elastoplastic strengthening, and damage-reduction phases. While the BASE and TSP-1 hysteresis curves with skin plates exhibit a well-defined skin effect and display a relatively stable post-peak performance, the TSP series from TSP-2 onward manifests a more rapid decline in load-bearing capacity. The inclusion of skin plates noticeably boosts the load-bearing potential of the joints.

Upon comparing the BASE and TSP series, we found that the yield loads for TSP-1, TSP-2, TSP-3, and TSP-4 declined by 2.8%, 6.0%, 10.02%, and 22.3%, respectively, when compared to the BASE specimen. Additionally, TSP-4 experienced a drop in yield and ultimate displacement by 26.3% and 14.9%, respectively, when compared with the BASE specimen. Therefore, to balance ductility and load-bearing capability at the joints, we recommend that the thickness of the skin plates should exceed half the thickness of the end-plate.

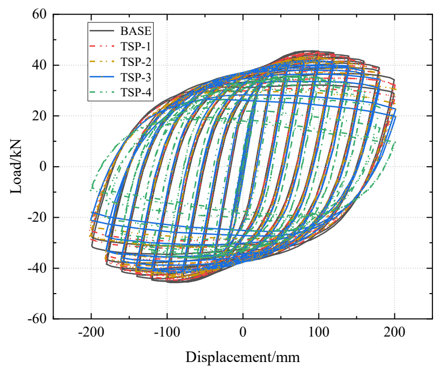

(a) Comparison of TSP series *P–Δ* hysteresis curves

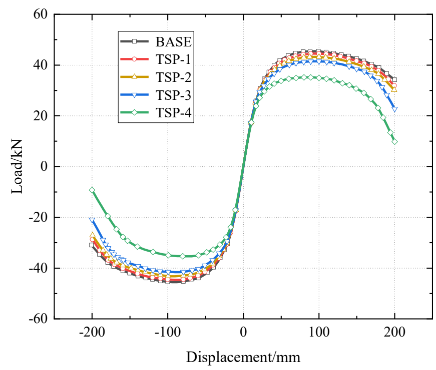

(b) Comparison of TSP series hysteresis skeletons

Fig. 19 Comparison of TSP series hysteresis curve and skeleton

Table 5
Bearing capacity, displacement, and ductility of TSP series specimens

Model number	Initial stiffness kN/mm^{-1}	Yield load P_y/kN	Yield displacement Δ_y/mm	Peak load P_{max}/kN	Limit displacement Δ_u/mm	Ductile coefficient μ
BASE	1.75	37.91	35.03	45.41	181.97	5.19
TSP-1	1.75	36.86	34.55	44.54	180.60	5.25
TSP-2	1.74	35.65	33.38	43.20	180.13	5.40
TSP-3	1.73	34.11	32.04	41.61	173.23	5.41
TSP-4	1.70	29.47	25.80	35.237	154.90	6.00

6.5. Influence of column-flange stiffener plate thickness

The hysteresis curves, skeleton curves, and mechanical properties of the TFS series are delineated in Fig. 20 and Table 6. The finite element analysis reveals that with the exception of TFS-5, hysteresis curves for the various joints approach fullness, indicating a drop in load-bearing capacity after reaching peak loads. Moreover, the rate of this decline remains fairly stable across joints, except for TFS-5.

Through a comparative analysis between the BASE and TFS series, the data show that the yield loads for the TFS series vary by -15.5%, -8.0%, 8.8%, 17.4%, and 24.6% when compared to the BASE specimen. Similarly, peak load variations for the TFS series, in relation to the BASE specimen, are -14.2%, -7.0%, 7.3%, 13.7%, and 18.8%. These numbers signify a boost in load-bearing capacity corresponding with increased thickness of the column-flange strengthening plates.

As for yield displacements, the TFS series exhibits variations of -8.9%, -5.0%, 5.1%, 8.7%, and 10.0% compared to the BASE specimen. The ultimate displacements of the TFS series show variations of -4.7%, -2.5%, 3.5%, 0.3%, and -20.6% relative to the BASE specimen. These findings reveal enhanced deformability with increasing thickness of the column-flange stiffener plates. To balance this improvement with other performance metrics, it is recommended that the thickness of the stiffener plates not exceed 0.8 times that of the end-plate.

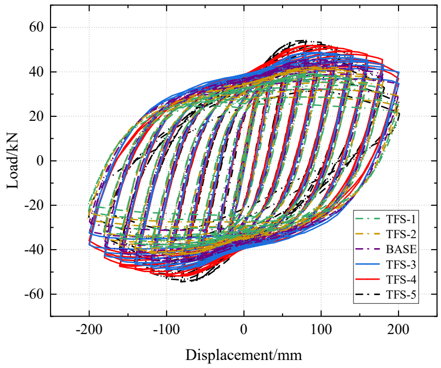

(a) Comparison of TFS series *P–Δ* hysteresis curves

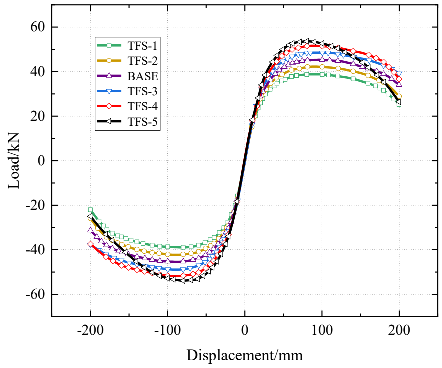

(b) Comparison of TFS series hysteresis skeletons

Fig. 20 Comparison of TFS series hysteresis curve and skeleton

Table 6
Bearing capacity, displacement, and ductility of TFS series specimens

Model number	Initial stiffness kN/mm^{-1}	Yield load P_y/kN	Yield displacement Δ_y/mm	Peak load P_{max}/kN	Limit displacement Δ_u/mm	Ductile coefficient μ
TFS-1	1.62	32.04	31.91	38.94	173.37	5.43
TFS-2	1.70	34.87	33.29	42.23	177.51	5.33
BASE	1.75	37.91	35.03	45.41	181.97	5.19
TFS-3	1.79	41.25	36.83	48.73	188.33	5.11
TFS-4	1.83	44.50	38.08	51.66	182.49	4.79
TFS-5	1.86	47.24	38.55	53.96	144.57	3.75

6.6. Influence of beam end-plate thickness

To investigate the seismic performance of the joint under different end plates, the variable parameter test is carried out under different end plate thicknesses, and the results are as follows:

Turning to the BEP series, Fig. 21 and Table 7 outline their hysteresis curves, skeleton curves, and mechanical properties. Our findings reveal that as end-plate thickness increases, shear deformation in the joint region tends to diminish. For the BEP series, specimens 1–3 and the BASE specimen show complete hysteresis patterns, accompanied by a relatively stable decline in load-bearing capacity. On the contrary, BEP-4 and BEP-5, while displaying enhanced load-bearing capacities, also exhibit pinching phenomena in their hysteresis curves.

Comparing the BASE and BEP series reveals that yield loads in the BEP series specimens exhibit variations of -8.3%, 11.4%, 20.9%, 27.6%, and 28.4%. In terms of ultimate displacements, these variations range from -2.0%, 2.2%, 6.1%, 2.3%, and -27.7%. The data suggest that increased BEP thickness enhances the structure's deformability. Consequently, we recommend an end-plate thickness equal to twice the column-flange thickness.

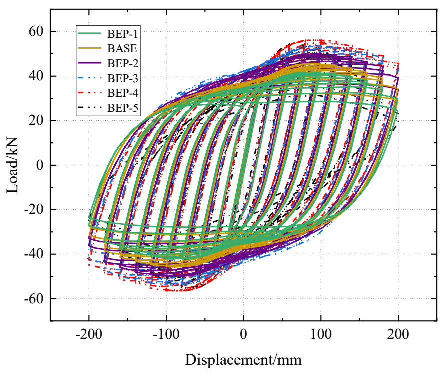

(a) Comparison of BEP series *P–Δ* hysteresis curves

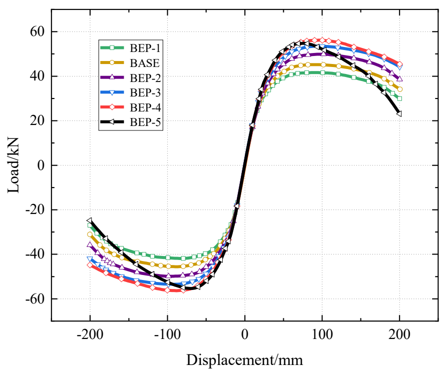

(b) Comparison of BEP series hysteresis skeletons

Fig. 21 Comparison of BEP series hysteresis curve and skeleton

Table 7
Bearing capacity, displacement, and ductility of BEP series specimens

Model number	Initial stiffness kN/mm^{-1}	Yield load P_y/kN	Yield displacement Δ_y/mm	Peak load P_{max}/kN	Limit displacement Δ_u/mm	Ductile coefficient μ
BEP-1	1.71	34.78	32.23	41.76	178.27	5.53
BASE	1.75	37.91	35.03	45.41	181.97	5.19
BEP-2	1.79	42.24	38.33	49.94	185.91	4.85
BEP-3	1.81	45.84	40.48	53.45	193.07	4.77
BEP-4	1.83	48.39	41.91	56.25	186.17	4.44
BEP-5	1.85	48.66	39.20	54.86	131.58	3.35

7. Conclusion

In summary, this study executed both experimental and numerical simulations to investigate the seismic behavior of a narrow-flange H-shaped beam-column structure equipped with endplates. Notably, the finite element models closely mirrored the experimental data, enabling in-depth parametric analyses of critical joint components. A refined resilience model was subsequently established, drawing from a wide array of finite element analyses. The conclusions are as follows:

(1) Experimental data showed that the hysteresis curve of the studied joint takes on a predominantly full, spindle-shaped form. The maximum equivalent viscous damping coefficient reached 0.43, underlining excellent energy dissipation performance. With peak loads of 73 kN, ultimate displacements of 198 mm, and a ductility coefficient exceeding 3.6, the joint demonstrates both strong load-bearing and ductile deformation capabilities. It is thus well-suited for use in mid-to-low-rise steel frame structures.

(2) There exists a negative correlation between the load-bearing capacity of the joints and the ACR. Specifically, as the ACR rises, the hysteresis curve exhibits a steeper negative slope. Therefore, it is advised that the ACR not surpass 0.4. When TCW thickness remains at or below 8 mm, the hysteresis curve exhibits well-defined features, maintaining stable load-bearing capacity and effective energy dissipation. As such, a column web thickness of 8 mm in the joint region is recommended.

(3) Increasing TSP thickness in the joint region benefits both the initial rotational stiffness and the energy dissipation capacity of the joint. Conversely, augmenting the thickness of the column-flange stiffener plate has the effect of diminishing the joint's initial rotational stiffness. To strike a balance between robust load-bearing capacity and optimized performance, we recommend a skin plate thickness that is 0.5 of the end-plate thickness. Additionally, the thickness of the strengthening plates should not exceed 0.8 times that of the end-plate.

(4) As the thickness of the end-plate increases, so does the joint's load-bearing capacity. However, there is a caveat: when the BEP thickness becomes overly substantial, the failure mechanisms transitions to BEP buckling. This change leads to only a marginal improvement in load-bearing capacity and a sharp decline in the structure's resilience to damage. To mitigate this, it is advisable to set the end-plate thickness at double the beam flange thickness.

Declaration of competing interest

The authors declare that they have no known competing financial interests or personal relationships that could have appeared to influence the work reported in this paper.

Acknowledgments

The National Natural Science Foundation of China provided funding for this research (Nos. 52408211, 52178162) and China Postdoctoral Science Foundation Funded Project (No. 2024MD764004). The authors also wish to express their gratitude for the financial support received from the scientific research plan projects of Shaanxi Education Department (Nos. 20JY033, 20JK0713).

References

[1] Hao J.P., Sun X.L., Xue Q., et al., "Research and Applications of prefabricated Steel structure building Systems", Engineering Mechanics, 34(01), 1-13, 2017. (in Chinese)
[2] Zhou X.H., Wang Y.H., "Status, problems and countermeasures of industrialization development of steel structural residence in China", Journal of Civil Engineering, 52(01), 1-7, 2019. (in Chinese)
[3] Wang J., Brian U., Thai H.T., et al., "Behaviour and design of demountable beam-to-column composite bolted joints with extended end-plates", Journal of Constructional Steel Research, 144, 221-235, 2018.
[4] D'Aniello M., Tartaglia R., Costanzo S., et al., "Seismic design of extended stiffened end-plate joints in the framework of Eurocodes", Journal of Constructional Steel Research, 218, 512-527, 2017.
[5] Haghollahi A., Jannesar R., "Cyclic Behavior of Bolted Extended End-Plate Moment Connections with Different Sizes of End Plate and Bolt Stiffened by a Rib Plate", Civil Engineering Journal, 4(01), 200-211, 2018.
[6] Hoang V.L., Jaspart J.P., Demonceau J.F., "Hammer head beam solution for beam-to-column joints in seismic resistant building frames", Journal of Constructional Steel Research, 103, 49-60, 2014.
[7] Chen S.F., "The Strength and stiffness of bolted connection in Portal Frame", Steel structure, 15(01), 6-11, 2000. (in Chinese)
[8] Guo B., Gu Q., Liu F., "Experimental study on hysteretic behavior of beam-column end-plate joints", Journal of Building Structure, 23(03), 8-13, 2002. (in Chinese)
[9] Li G.Q., Duan L., Lu Y., "Experimental and theoretical study of bearing capacity for extended endplate connections between rectangular tubular columns and H-shaped beams with single direction bolts", Journal of Building Structure, 36(09), 91-100, 2015. (in Chinese)
[10] Wang Y., Li H.J., Li J.F., et al., "Analysis of initial stiffness and structural internal forces of semi-rigid beam-column joint connection". Engineering Mechanics, 20(06), 65-69, 2003. (in Chinese)
[11] Tong G.S., Zhao W., "Design Approach of Stiffeners in Extended End Plate Connections and Finite Element Analysis", Journal of Shenyang Jianzhu University (Natural Science), 21(06), 616-620, 2005. (in Chinese)
[12] Zhong W.H., Zhao M.J., Zhou L., et al., "Seismic performance of a narrow flange H-beam-to-column full-bolt end-plate weak-axis connection". Structures, 46, 637-653, 2022.
[13] "Standards for design of steel structures: GB 50017—2017", Beijing: China Architecture & Building Press, 2017. (in Chinese)
[14] Guo B., Guo B.S., Zhang H.W., "M-θ relations for extended end-plate beam-column bolted connections", Journal of Shandong Institute of Arch and Eng, 16(03), 1-5, 2001. (in Chinese)
[15] Solhmirzaei A., Tahamouli R.M., Hosseini H.B., "A new detail for the panel zone of beam-to-wide flange column connections with endplate", Structures, 34, 1108-1123, 2021.
[16] AISC (American Institute of Steel Construction). Prequalified connections for special and intermediate steel moment frames for seismic applications. AN-SI/AISC 358–16, Chicago, IL, 2016.
[17] Tartaglia R., D'Aniello M., Gian A.R., et al., "Full strength extended stiffened end-plate joints: AISC vs recent European design criteria", Engineering Structures, 159, 155-171, 2018.
[18] Technical code for steel structure of light-weight building with gabled frames GB 51022—2015 [S] Beijing: China Architecture & Building Press, 2017. (in Chinese)
[19] Lu L.F., Li C.C., Liu Z.L., et al., "Finite element analysis of the strengthen-joint region connection of I-shaped columns for the strong axis", Advanced Civil, Urban and Environmental Engineering, 157, 123-131, 2014.
[20] "Earthquake resistant design code GB 50011-2010", Beijing: China Architecture & Building Press, 2016. (in Chinese)
[21] "Steel and steel products—Location and preparation of samples and test pieces for mechanical testing GB/T 2975-2018", Beijing: Standards Press of China,2018. (in Chinese)
[22] FEMA-267A. Interim Guideline: Advisory No. 1, Supplement to FEMA-267A[R]. Rep. SAC Joint Venture, Sacramento, California, 1997.
[23] Tan Z., Zhong W.H., Tian L.M., et al., "Quantitative assessment of resistant contributions of two-bay beams with unequal spans", Engineering Structures, 242, 112-445, 2021.
[24] Zhong W.H., Tan Z., Tian L.M., et al., "Collapse resistance of composite beam-column assemblies with unequal spans under an internal column-removal scenario", Engineering Structures, 206, 110-143, 2020.
[25] Tan Z., Zhong W.H., Gao Y., et al., "Collapse behavior of unequal-span multistory composite frames under the scenario of removing an internal column", Journal of Structural Engineering, 150(12), 04024173, 2024.
[26] ABAQUS, Analysis User's Manual, 6.17, ABAQUS, Inc., Dassault Systemes, USA, 2017.